# The built-in capacity of CT D'OR's static ring for scatter correction

Helmut Schlattl and Christoph Hoeschen

Helmholtz Zentrum München – German Research Center for Environmental Health, Institute of Radiation Protection, Ingolstädter Landstr. 1, 85764 Neuherberg

#### ABSTRACT

The new scanner geometry CT D'OR ("CT with Dual Optimal Reading"), developed at the Helmholtz Zentrum München (former GSF - National Research Center for Environment and Health), consists of a discontinuous ring of detectors facing toward the ring center, which are fixated on an x-ray absorbing material. The x-ray source and an additional outer detector are mounted on a gantry which rotates around the inner static detector and thus the patient. When the source is moving, the detectors are alternately exposed and shielded from the source. Data recorded during periods of direct exposure can be combined and are used for the reconstruction of the image. When the detectors are shielded, their signal is solely caused by scatter. Therefore, direct scatter correction is possible. This can be used to considerably improve the image quality, when scatter radiation yields a strong deterioration of the reconstructed image. The advantage of CT D'OR is thus, that information about scatter radiation is obtained without additional effort or exposure. This property of CT D'OR is investigated and its feasibility is demonstrated by the use of Monte Carlo simulations.

# Keywords: SCAT, CT, SIM

# 1. INTRODUCTION

In the last years, x-ray based computed tomography has evolved from single- to multi-row detector systems leading to basically less acquisition time and thus less artifacts due to patient movements. However, with growing cone angle, the number of scattered photons recorded in the detector has substantially increased, which leads, for instance, to the well known cupping artifacts.<sup>1–3</sup> This issue will become even more critical with forthcoming CT system which will use a large flat panel detector. A lot of effort has been spent in correcting the detector signal by numerous models or measurements of the distribution of scatter radiation.<sup>4–8</sup> A newly proposed CT scanner geometry, named CT D'OR,<sup>9</sup> has the capacity to overcome this problem by directly measuring the scattered radiation without considerable additional effort, while the radiation dose to the patient could be reduced considerably. More details about the advantages of CT D'OR can be found in Ref. [10].

The scatter-correction capacity of CT D'OR is demonstrated with the help of a Monte Carlo transport code. It allows to distinguish between scatter and primary radiation and thus enables to access the quality of the scatter-correction scheme. The irradiation of a virtual phantom in a CT D'OR scanner geometry with a large detector is simulated, and reconstructed images with and without scatter correction are compared.

#### 2. COMPONENTS

# 2.1 Scanner geometry

The geometry of CT D'OR is illustrated in Fig. 1a. The arrangement of the two detector rings is chosen such, that each photon which is transmitted through the object is also recorded in one of the two detectors. More details about the advantages of this scanner geometry together with the reconstruction algorithm OPED ("Orthogonal Polynomial Expansion on the Disk") are described elsewhere. <sup>10–12</sup> From Fig. 1a it is obvious, that not every detector is exposed to direct radiation from the source at a fixed source position. For instance, at the shown position, the detectors directly opposite of the source do not record any direct radiation, but they do record scatter radiation. Apparently the detectors of the outer ring are also partly shielded by the inner ring, such that they receive much less scatter radiation. Therefore, in this work, only the static ring is examined, although in the future the signals in the outer ring might also be used for a further improvement of the scatter correction.

For the presented simulations, the diameters of source and detector rings have been chosen to be 100 and 70 cm, respectively; the detector height is 30 cm (see also Sec. 3.1).

Correspondence to H.S. (helmut.schlattl@helmholtz-muenchen.de)

Medical Imaging 2008: Physics of Medical Imaging, edited by Jiang Hsieh, Ehsan Samei, Proc. of SPIE Vol. 6913, 691352, (2008) · 1605-7422/08/\$18 · doi: 10.1117/12.769426

Proc. of SPIE Vol. 6913 691352-1

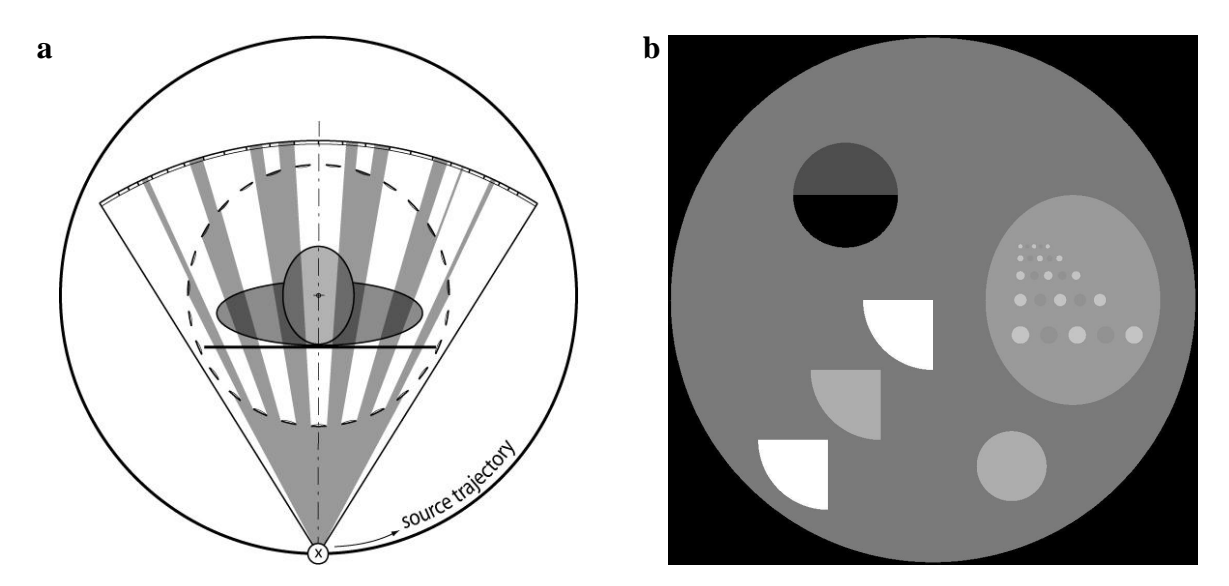


Figure 1. a) Sketch of the CT D'OR scanning principle. Around the object (patient) a static holey detector ring is assembled, where the back of each detector is covered by a shielding material to block the x-rays. Photons which are transmitted through the patient, but are not recorded by the inner static ring, are impinging on an outer detector array. This array is mounted together with the x-ray tube on the gantry and thus is rotates together with the source around the patient. b) Gray-scale image of the applied model. The gray values scale linearly with the the mass energy-absorption coefficient for an x-ray spectrum of 120 keV and a HVL of 8.25 mm Al. However, for the illustration the absorption of the mineral-bone wedges has been strongly reduced, such that the whole image appears brighter than in a real CT image, and low-contrast objects like the circles of water in the ellipse are better visible.

#### 2.2 Virtual model

A transverse slice of the virtual phantom used in the simulations is shown in Fig. 1b. The phantom has a diameter and height of 30 cm, where the structure is not changing with height. The phantom is filled with adipose tissue and contains a circle in the upper left is filled half with air and half with lung tissue. In the right half an ellipse filled with some soft tissue is embedded, which contains small circles of different sizes, filled alternately with water and slightly over-dense cartilage ( $\varrho = 1.2 \text{ g/cm}^3$ ). A small circle filled with original cartilage ( $\varrho = 1.1 \text{ g/cm}^3$ ) tissue can be found at the lower right. In the lower left region, the model contains three wedges, where the central one is composed of original cartilage and the others of mineral bone.

#### 3. METHODS

### 3.1 Numerical simulation

The transmission, absorption and scattering of x-rays through the model is determined with the help of the Monte Carlo transport code EGSnrc. The scatter-correction capability of CT D'OR is demonstrated by reconstructing the central slice of a system with large detectors employing the OPED reconstruction algorithm. However, the large cone angle would demand a huge number of photons to be followed until a sufficient number of scattered photons is obtained in the central detector row. Moreover, only a very small portion of the photons leaving the object is impinging on the central row, so that most of them are not used in the analysis. An optimal photon yield can be obtained by applying the radiation reciprocity principle, employing the inverse configuration in the simulations. There, a 2-dimensional fan beam is used and the detector signal is summed over each row. Thus, a considerable photon statistics is achievable within acceptable computation time. For the simulations, each detector has a height of 30 cm to collect nearly all scattered photons.

In the Monte Carlo simulation, each particle which undergoes photo-effect, Bremsstrahlung, Compton or Rayleigh scattering is marked and counted separately from the unattenuated photons in each detector. Hence, the optimal image, which would have been obtained without scatter radiation, can be determined, and the quality of the scatter-correction scheme be assessed.

The detector response is assumed to be linearly decreasing with the energy, with an efficiency of 32% at 50 keV and 24% at 75 keV. This values have been derived from DQE measurements of a GI Revolution XQI detector performed according to the standard IEC-62220-1. The energy spectrum of the chosen x-ray source corresponds to a tube voltage of 120 kV with a filtration of 1.2 mm Ti and 1.5 mm Al.

Two different simulations have been performed. In a first one, a homogeneous phantom with a diameter of 30 cm has been employed to demonstrate the patterns in the scatter-radiation signal described in Sec. 3.3. This model was filled completely with adipose tissue. The number of detector-slit pairs was 101. In total 28.8 billion initial photons have been followed through the object, equally distributed over the source ring. The fan angle was 35.53°, fully covering the object.

In a second experiment, a full scan of the test object (Fig. 1b) with 501 detector-slit pairs has been simulated, pursuing in total the history of 173 billion source photons within a fan of 35.33°. The resulting data set has been used to perform the presented scatter-correction scheme (Sec. 3.3), and compute reconstructed images employing the OPED reconstruction algorithm.

# 3.2 OPED reconstruction

The CT D'OR scanning geometry has been developed to provide an optimal usage of the x-ray attenuation data and the resulting data are perfectly arranged for the OPED<sup>11</sup> reconstruction algorithm. Since, here only the data of the static ring are used, its parallelized data can be directly used with OPED without further interpolations. In Fig. 2a one parallel data set is illustrated for the optimal case of equally sized detectors and slices. In this case, the whole scanning area is covered by x-rays. As required by OPED, the number of strips is denser close to the edges. This also implies that the strips are not equally thick, which leads to different detector signals, even when no object is attenuating the x-ray intensity. As the

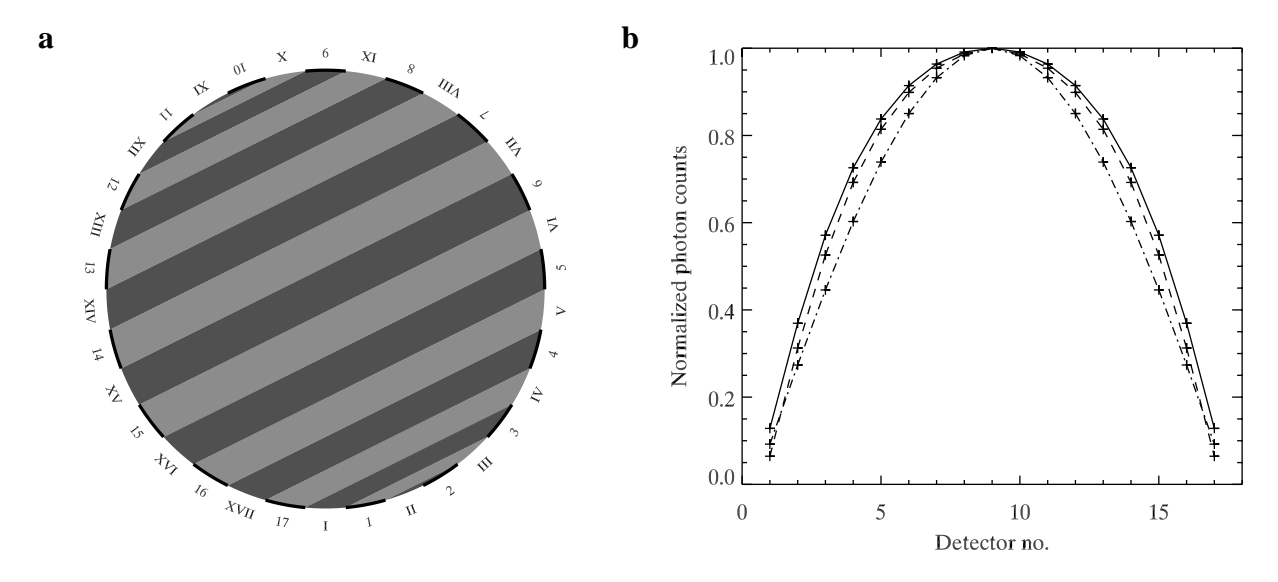


Figure 2. a) Illustration of the x-ray coverage of parallelized data set of the static ring (after a full rotation) with 17 slit/detector pairs. Each strip between a slit (Roman numbers) and a detector (Arabic numbers) represents the area covered by x-rays. b) Correction factors for the detector signal. The number of photons detected at each detector for photons passing through slit I  $(n_{\rm ph}^{1,i},$  Eq. 1) are indicated by the points connected with the solid line. Here, a system with 17 detector/slit-pairs and a source-to-detector-ring diameter-ratio of 0.7 has been chosen. For comparison, the strip thickness is shown by the points connected by the dash-dotted line. In addition, the opening angle has been determined, under which the detector appears from the position in the center of the respective source region  $(\phi = (\phi_{\rm s}^{1,j} + \phi_{\rm t}^{1,j})/2$ , see below). This quantity is represented by the points connected by the dashed line. All quantities are normalized to their value at detector no. 9.

algorithm does not account for the different thicknesses, it has to be corrected for:

$$\tilde{S}^{i,j} = S^{i,j} / \tilde{n}_{\rm ph}^{i,j}$$
 with

 $\tilde{n}_{\rm ph}^{i,j} := n_{\rm ph}^{i,j} / n_{\rm ph}^{1,(n+1)/2}$  and

 $n_{\rm ph}^{i,j} = n_{\rm ph}^{1,j-i+1}$ 

where  $S^{i,j}$  and  $\tilde{S}^{i,j}$  are the measured and corrected detector signal, respectively, and  $n_{\rm ph}^{i,j}$  the number of photons contributing to the strip from slit i to detector j (without object).

Unfortunately,  $n_{\rm ph}^{i,j}$  is not simply proportional to the strip thickness, as one might assume initially. The actual x-ray source provides a diverging beam and thus the photon density is decreasing with increasing source-detector distances. Therefore,  $\tilde{n}_{\rm ph}^{i,j}$  can hardly be determined analytically. Anyway, for large detector numbers, those source positions which contribute to a strip do not vary considerably. Thus, a good approximation for  $\tilde{n}_{\rm ph}^{i,j}$  can be achieved by determining the opening angle under which the detector appears for the respective central source position, which belongs to an individual strip. In Fig. 2b a comparison of the different "correction" factors is given, where the points connected by the solid line represent  $\tilde{n}_{\rm ph}^{i,j}$ , where the total photon counts for each strip have been summed numerically. Note, that already for this low number of slit-detector-pairs a very good approximation to  $\tilde{n}_{\rm ph}^{i,j}$  is achieved by using the opening angle. And this approximation is considerably better than using the strip thickness.

The presented corrections for the detector signals are necessary for a consistent image reconstruction, and resemble a calibration of the detectors. They are independent of whether any further corrections to improve the image quality, like scatter corrections, are applied.

#### 3.3 Scatter correction

When only a single detector is considered, it can be noticed that exposed and shielded periods are alternating when the source is moving around the object (see Fig. 3a). The scatter contribution of the signal during an exposure period can then be estimated by the signal at the two neighboring shielded positions. This method is similar to the one described in a previous work,<sup>6</sup> where a co-rotating shielding mask as in Fig. 3b has been employed. However, the fixed mask of CT D'OR leads to some differences to the case with co-rotating mask.

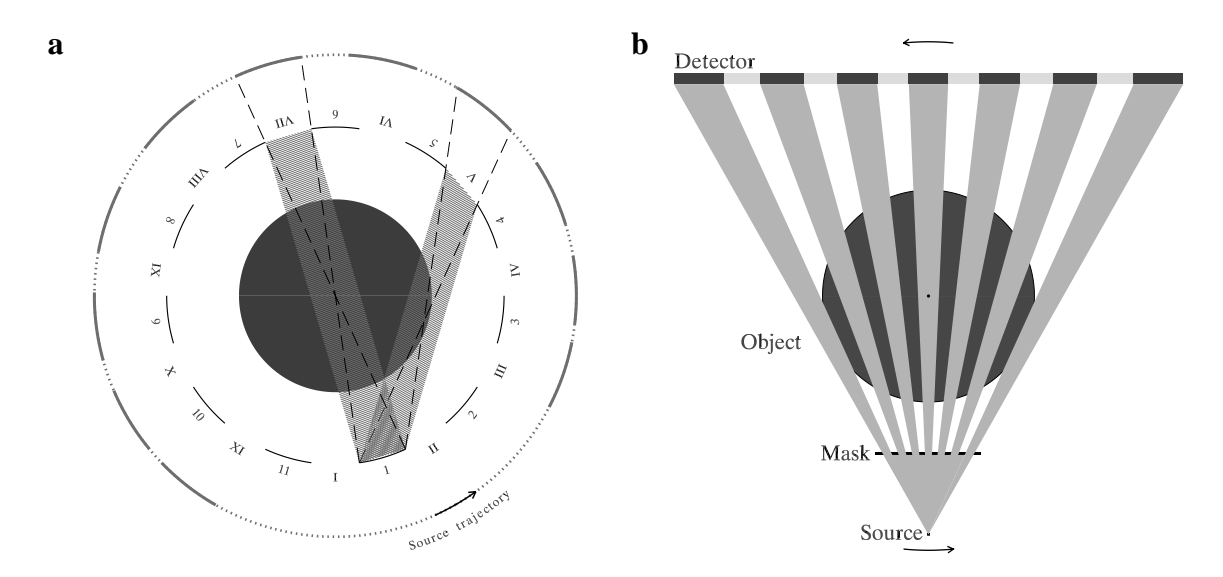


Figure 3. a) Illustration of CT D'OR with 11 pairs of slits/detectors. At the outer (source) ring, those regions are marked, where detector no. 1 is exposed to direct radiation through the respective slit. As examples, the two pairs of dashed lines indicate the first and last ray, respectively, which can directly reach detector no. 1 through slit V or VII. The gray hatched areas show the whole area which is covered by x-rays through slit V and VII impinging on detector no. 1. b) Sketch of a gantry with a co-rotating mask for comparison.

First of all, the periods of exposure and shielding of a single detector are not simply direct proportional to the slit or detector width. The angular range  $\phi^{i,j} = [\phi_{\rm S}^{i,j}, \phi_{\rm E}^{i,j}]$ , where a detector j is exposed through slit i is given by the following formula:

$$\phi_{S,E}^{i,j} = \phi_{S,E}^{i-j+1,1} + 4(j-1)\tau \tag{2}$$

where  $\tau = \pi/(2N)$  with N being the number of detectors (or slits). The angular range for detector no. 1 is given by

$$\phi_{\rm S}^{i,1} = (2i - 1 - \zeta_+)\tau + \arccos\left\{\frac{r_{\rm D}}{r_{\rm S}}\cos\left[(2i - 3 - \zeta_-)\tau\right]\right\}$$
 (3)

$$\phi_{\rm E}^{i,1} = (2i - 1 + \zeta_+)\tau + \arccos\left\{\frac{r_{\rm D}}{r_{\rm S}}\cos\left[(2i - 3 + \zeta_-)\tau\right]\right\}$$
 (4)

with  $r_{\rm D}$  and  $r_{\rm S}$  being the radius of the detector and source ring, respectively. Here,  $\phi$  is chosen such that the center of slit I is at  $\phi = 0$ .

$$\zeta_{\pm} = \frac{1 \pm \eta f}{1 + f},\tag{5}$$

where f is the ratio of shielding width to slit width and  $\eta$  the portion of the shield covered by the detector. The simplest case with  $f = \eta = 1$  as illustrated in Fig. 3a yields  $\zeta_+ = 1$  and  $\zeta_- = 0$ , and thus

$$\phi_{\rm S}^{i,1}(f=\eta=1) = 2(i-1)\tau + \arccos\left\{\frac{r_{\rm D}}{r_{\rm S}}\cos\left[(2i-3)\tau\right]\right\}$$
 (6)

$$\phi_{\rm E}^{i,1}(f=\eta=1) = 2i\tau + \arccos\left\{\frac{r_{\rm D}}{r_{\rm S}}\cos\left[(2i-3)\tau\right]\right\}.$$
 (7)

Hence, in this case the angular period for exposure  $\phi_{\rm E}^{i,j}-\phi_{\rm S}^{i,j}=2\tau$  is constant. However, this does not apply to the period of shielding  $\phi_{\rm S}^{i+1,j}-\phi_{\rm E}^{i,j}$ , which can also be recognized in Fig. 3a.

Nevertheless, with Eqs. 2-5 it is possible to normalize the signal of the exposure or shielding periods. Hence, the scatter signal of a detector during two shielded periods can be used to determine the scatter portion during the exposure period in between.

However, possibly not only the period of the exposure or shielding must be corrected for in CT D'OR. In this geometry, the amount of radiation which impinges on the object, and thus could yield to scatter radiation, is not simply depending on

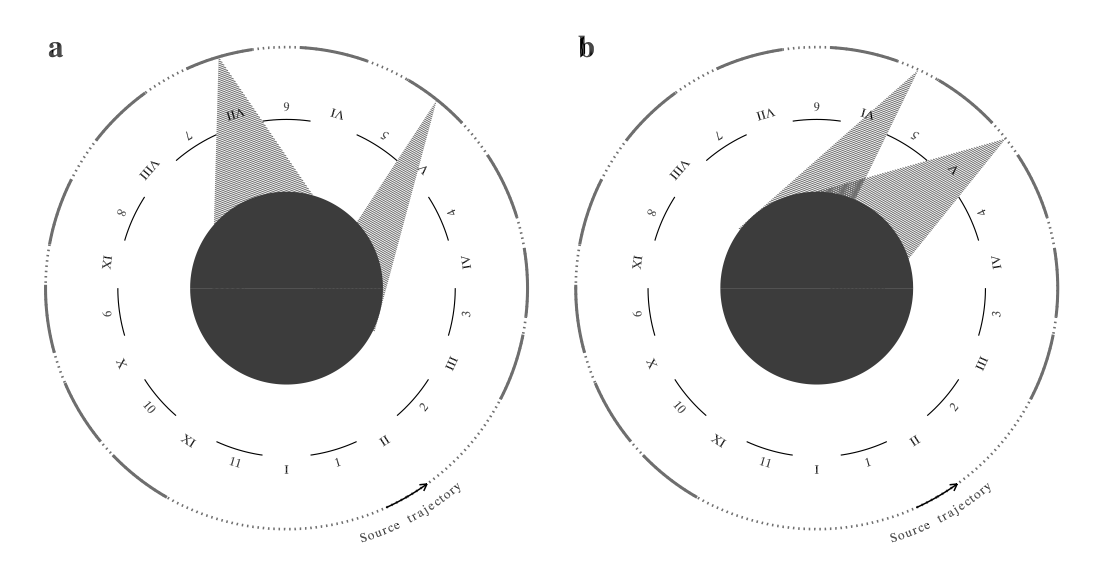


Figure 4. Beam portion penetrating the object in the central position, when detector no. 1 is exposed to slit V or VII (a) or is shielded by detector no 4 or 5 (b). The beam portion influences the amount of scatter produced in the object and thus the signal or signal contribution of scatter radiation in the detector.

the slit or detector width as for the co-rotating mask, but has an odd dependence on the source position and the object size. This behavior is illustrated in Fig. 4 for detector no. 1. For simplicity only the radiation from the central position of the exposed or shielded angular range is shown.

Noticeably, the opening angle of the fan impinging on the object is much smaller when detector no. 1 is exposed through slit V than through slit VII (Fig. 4a). Similarly, also during the periods when detector no. 1 is shielded, the amount of radiation impinging on the object can depend considerably on the source position as demonstrated in Fig. 4b. In a first approximation, one can assume that the recorded scatter radiation is proportional to the total number of photons which are able to hit the object during periods of shielding and exposure, respectively. These numbers can then be used to normalize the scatter-radiation signal and to perform the scatter correction. For instance, let  $\nu_V$ ,  $\nu_4$  and  $\nu_5$  be the described photon numbers, when detector no. 1 is exposed through slit V or shielded by detector no. 4 or 5. The corresponding detector signals are denoted by  $S_V$ ,  $S_4$ , and  $S_5$ , respectively. Then, the primary signal  $S_V^{\text{prim}}$  during slit-V exposure can be estimated by

$$\begin{split} S_{\mathrm{V}}^{\mathrm{scat.}} &\;\; \approx \;\; \frac{\nu_{\mathrm{V}}}{2} \left( \frac{S_4}{\nu_4} + \frac{S_5}{\nu_5} \right) \\ S_{\mathrm{V}}^{\mathrm{prim.}} &\;\; = \;\; S_{\mathrm{V}} - S_{\mathrm{V}}^{\mathrm{scat.}} \,. \end{split}$$

The drawback of this procedure is that the size of the object has to be known in advance, which is difficult to be determined for each patient in real CT scanners. However, for large slit/detector numbers N and sufficiently large objects, the photon numbers  $\nu$  become proportional to the angular periods described above, which can be determined analytically without knowledge of the object.

It is worth noticing that there are further problems with this procedure when the slit/detector numbers are small like in the example of Fig. 3a and Fig. 4. Firstly, a larger photon numbers  $\nu$  does not necessarily imply that the scatter-radiation signal is larger. For instance, the probability of scatter radiation to hit detector no. 1 is higher for slit-V than for slit-VII photons, as most slit-VII photons will be scattered back. Thus, detector no. 1 might record even less scattered photons through slit-VII than through slit-V although  $\nu_{\rm VII}$  is larger than  $\nu_{\rm V}$ . Secondly, the object area which is exposed to radiation during slit-V exposure hardly overlaps with the areas during detector-4 or detector-5 shielding. Thus scatter correction is hardly possible in this example. This would, however, also be the case with a co-rotating mask with large slits.

# 4. RESULTS AND DISCUSSION

The patterns in the scatter-radiation signal described in Sec. 3.3 are demonstrated by using a homogenous virtual model. In Fig 5a the result for the scatter signal in detector no. 1 is shown. Since the object is homogeneous, the same signal dependence is recorded in each detector, just the assignment to the respective slits is shifted. The solid line represents the detector signal during the periods, when it is shielded from direct exposure, and thus consists solely of scattered photons. This signal would also be measurable in a real system. The aim of the presented scatter-correction scheme is to reproduce the contribution of scatter in the signal during the periods, where the detector is exposed to the x-ray source. The dashed curve in Fig. 5a represents this scatter signal deduced from the simulations.

A prominent feature in the signal when the detector is shielded (solid line), is the orders of magnitude higher number of photon counts, when the source is behind the detector ("slit no." = 0.5). The main reason is the long period relative to the other ones, also noticeable in Fig. 3. When correcting for the different period lengths of exposure or shielding using Eqs. 6 and 7, both curves become much more similar (Fig. 5b). But still, the signals shows reasonably strong oscillations. Note, that for a perfect scatter correction, it would be necessary to reproduce the dashed curve by interpolating the solid one. As described in Sec. 3.3 the causes of the oscillations are the variation of the beam portions which are irradiating the object (Fig. 4) and the angular dependence of the scatter signal. We verified, that in this case, the angular dependence is the main source for the oscillations.

In a second simulation, a full scan of the test object (Fig. 1b) with 501 detector-slit pairs has been performed numerically. In Fig. 6a that image is displayed, which followed from the complete data set including scatter. If no scatter would have been present then Fig. 6b would be obtained. The well known cupping artifacts, i.e., the reduced brightness in the center, caused by the additional scatter signal, can be easily seen in Fig. 6a. Apparently, the cartilage wedge between the two mineral-bone wedges at the lower left part is hardly discernible, as well as most of the objects inside the ellipse

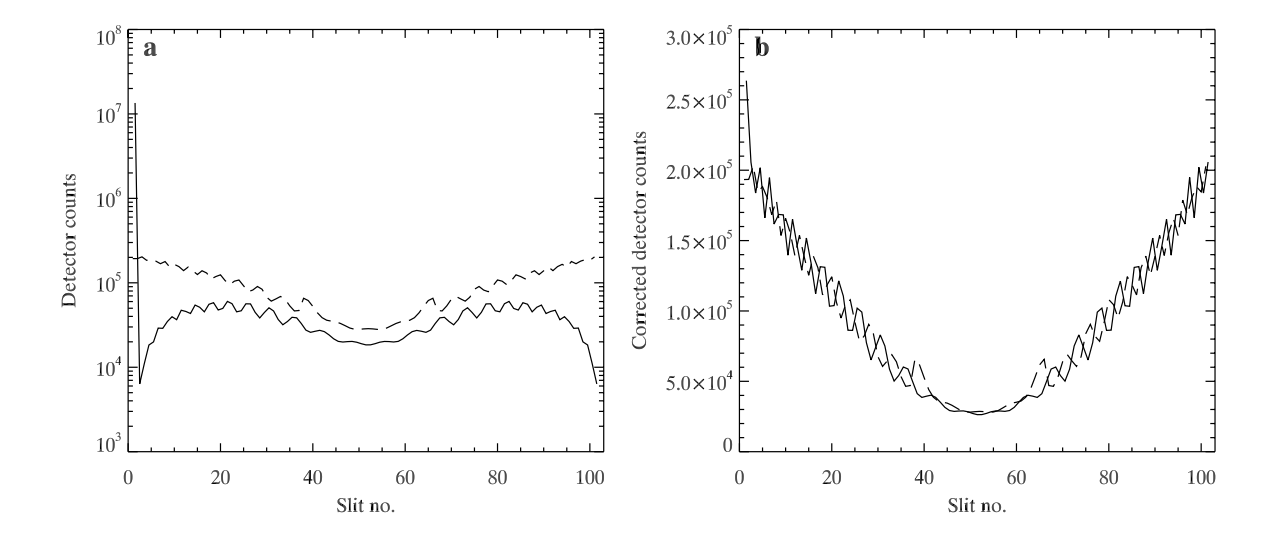


Figure 5. a) The detector signal for scatter radiation when the detector no. 1 is exposed (dashed line) through the various slits obtained from a Monte Carlo simulation (see text for more details). The scatter data between the exposure through two slits are shown by the solid line, where the slit number is then defined as the mean of the two neighboring slits. b) Similar to a), but correcting for the different angular periods for exposure and shielding.

disappear. In the scatter-free image the high dense regions like the wedges lead to some typical, and not unusual, streak artifacts.

When correcting the full signal of the exposed detectors with the signal from the shielded periods as proposed in Sec. 3.3, then Fig. 7a is obtained. A considerable improved contrast can be observed compared to Fig. 6a, but new ring-shaped artifacts have been introduced. The corresponding oscillations are also visible, when regarding just one row like in Fig. 8a. A possible reason for these artifacts could be that only the different period lengths of exposure and shielding

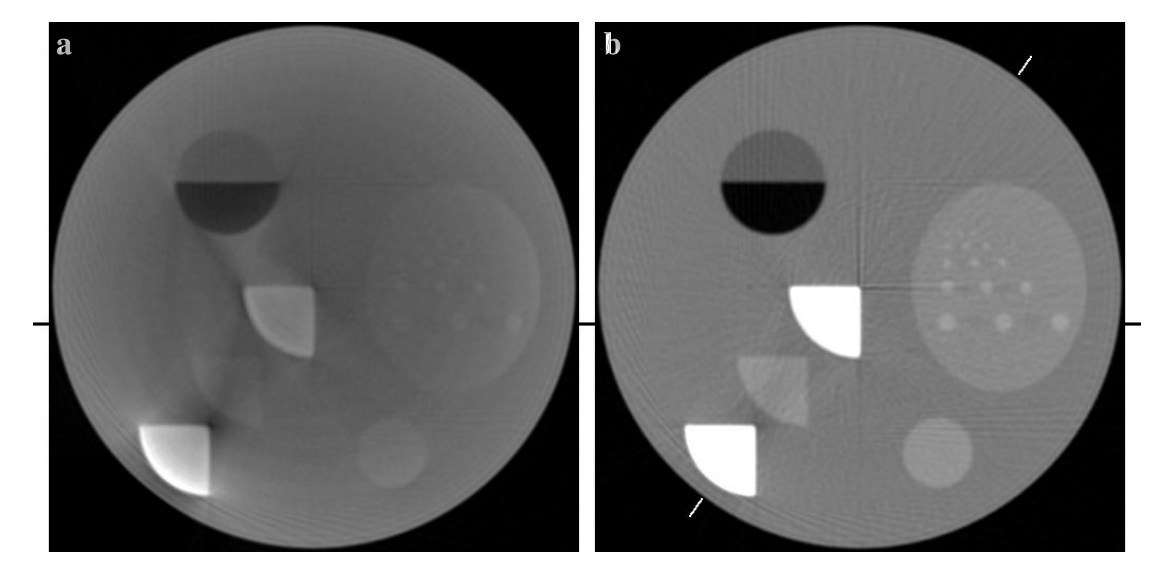


Figure 6. The reconstructed image  $(501 \times 501)$  resulting from the static-ring data of CT D'OR with (a) and without scatter radiation (b), i.e., the optimal case. An upper limit to the CT numbers have been set, to enhance the contrast for objects with lower CT numbers. The same relation between gray value and CT number is applied in both figures. The object and scanner dimensions are described in Sec. 2. In total, 501 detector-slit pairs have been used. The horizontal lines mark row no. 216, which is shown in more detail in Fig. 8a. The white lines in b) indicate the direction of the parallelized data set displayed in Fig. 8b.

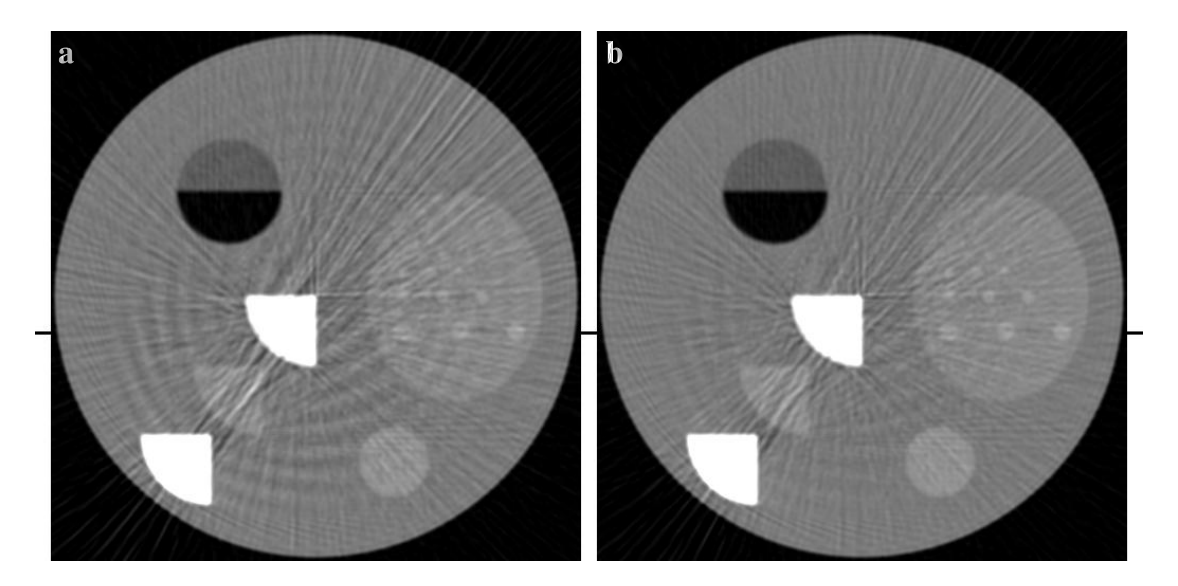


Figure 7. a) Reconstruction using the scatter-correction scheme described in Sec. 3.3, i.e., only accounting for the different period lengths of exposure and shielding. b) As a), but smoothing the scatter data before correcting the detector signals. The same relation between gray value and CT number is applied as in Fig. 6.

for a single detector has been accounted for. There has been made no correction for the object size, or the scatter-radiation directions. Thus, the oscillations in the scatter signal during exposure (cf. Fig 5b) certainly could not have been reproduced correctly by the signal, when the detectors were shielded. However, for 501 views this oscillations are much smaller than for 101 views as in Fig 5b. Thus, it is not expected that insufficiently correcting this oscillations can cause these rather strong artifacts. Currently, the source of ring artifacts has not been fully understood, and is still under investigation. Note, that similar artifacts can been observed in micro-CT systems, where they are caused by small differences in the detector response. <sup>16</sup>

Anyway, it is worth noticing, that in the chosen example, scatter radiation can contribute more than 90% to the total

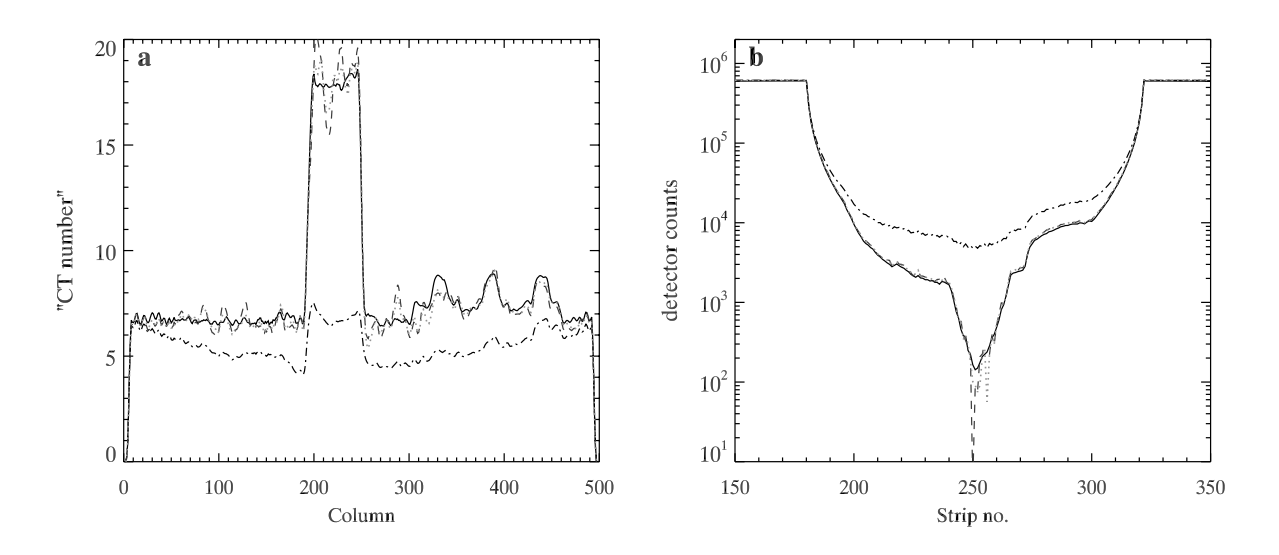


Figure 8. a) Row no. 216 of the reconstructed image using different data sets (note, the shown "CT number" is not in Hounsfield units), with scatter (dash-dotted), without scatter (solid), with scatter correction (dashed) and smooth scatter correction (dotted). b) The detector signal in the different strips parallel to the direction indicated in Fig. 6b using the same line styles as in a).

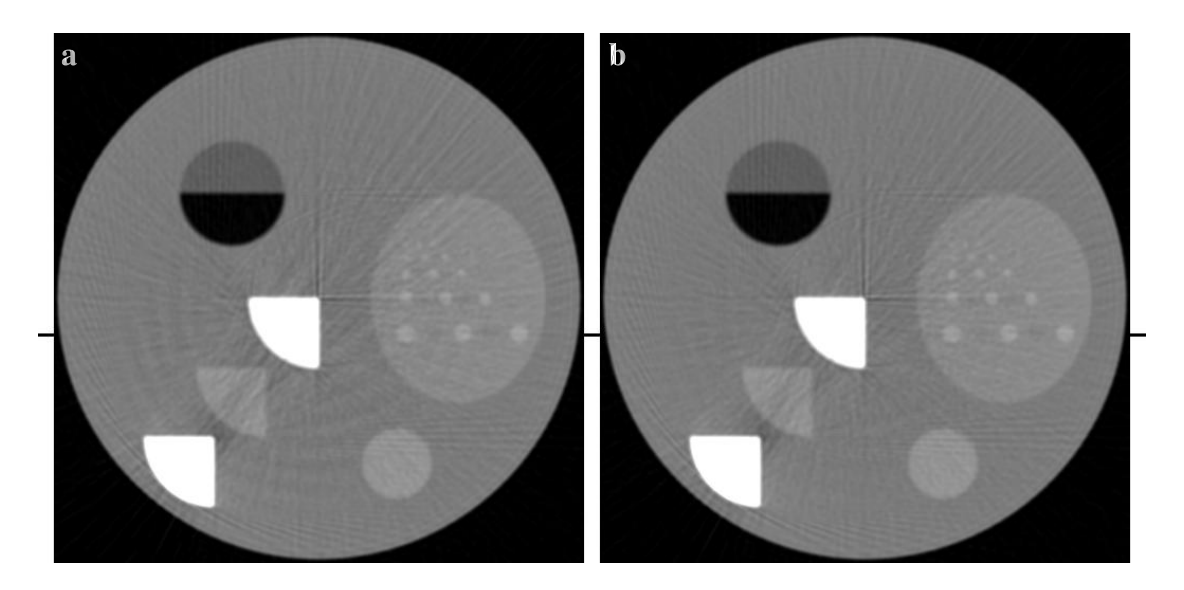


Figure 9. Similar to Fig. 7, but artificially decreasing the total scatter by 70%.

signal, particularly for strips (slit-detector pairs) which cover all three wedges. The high proportion of the scatter signal is demonstrated in Fig. 8b, where the parallelized (sinogram) data for the direction through the three wedges are shown for different data sets. Clearly, the signal from primary radiation (solid line) is a large factor smaller then the signal from scatter radiation. Thus, small errors made in the scatter-correction procedure can have a significant influence on the resulting sinogram data. For instance, for the central strip (about no. 250), the scatter correction leads to almost no primary signal at all (dashed line), which certainly will cause strong streak artifacts, also visible in Fig. 7a. So, in view of the large scatter-radiation signal and the resulting problems, the reconstructed image (Fig. 7a) is undoubtedly already a big improvement compared to the uncorrected image (Fig. 6a).

In a first attempt, for an image with less ring artifacts, the scatter data have been smoothed before being used to correct the signal. The resulting image (Fig. 7b) shows indeed much less ring and streak artifacts and there are still many details visible as, for instance, inside the ellipse.

With the presented simulation setup, the scatter contribution in a large detector with a height of about 30 cm is determined. In such a big detector almost all scatter radiation is recorded, at least in the central detector rows. This is thus probably the worst case, which the scatter-correction scheme has to cope with. To demonstrate the quality of the present scheme also in a less severe case, we artificially reduced the scatter signal by 70% through the data set, and then performed again the scatter correction as before. In Fig. 9 the resulting images are shown, where in the right panel an additional smoothing of the scatter data has been applied. A comparison of Fig. 9b with the image without scatter (Fig. 6) reveals an excellent agreement. Hence, for lower levels of scatter radiation, high-quality scatter correction in CT D'OR is indeed possible without any additional data required.

# 5. CONCLUSION

The new scanner geometry CT D'OR and its potential for scatter correction has been demonstrated. Furthermore, the specifics of this scanner geometries have been pointed out, which are mainly caused by the static ring-mask. In contrast to a co-rotating mask, this led to a variety of obstructions which have to be overcome before scatter correction can be performed. One peculiarity are the different periods of exposure and shielding for a single detector, which could be easily corrected for. Others, like the influence of the object size and the preferred direction of scatter radiation has been identified, but are difficult to be accounted for in a real CT scanning situation. For a large number of detector-slit pairs, their footprints in the scatter signal should however fade, such that they probably have not to be accounted for. Nevertheless, ring-shaped artifacts appear in images with scatter correction, the cause of which is not yet clear. It cannot be excluded that neglecting object size and preferred direction of scatter radiation in the scatter-correction scheme are still the cause for the artifacts. A more thorough investigation of the ring artifacts is certainly the next step to be tackled in the near future.

# REFERENCES

- [1] Johns, P. C. and Yaffe, M., "Scattered radiation in fan beam imaging systems," Med. Phys. 9, 231-239 (1982).
- [2] Joseph, P. M. and Spital, R. D., "The effects of scatter in x-ray computed tomography," Med. Phys. 9, 464–472 (1982).
- [3] Glover, G. H., "Compton scatter effects in CT reconstruction," Med. Phys. 9, 860–867 (1982).
- [4] Ning, R., Tang, X. and Conover, D., "X-ray scatter correction algorithm for cone beam CT imaging," Med. Phys. 31, 1195–1202 (2004).
- [5] Siewerdsen, J. H., Daly, M. J., Bakhtiar, B., Moseley, D. J., Richard, S., Keller, H. and Jaffray, D. A., "A simple, direct method for x-ray scatter estimation and correction in digital radiography and cone-beam CT," Med. Phys.33, 187–197 (2006).
- [6] Schlattl, H., Tischenko, O. and Hoeschen, C., "Modeling of realistic raw data for image reconstruction," Proc. SPIE 6142, 614256 (2006).
- [7] Bertram, M., Wiegert, J. and Rose, G., "Scatter correction for cone-beam computed tomography using simulated object models," Proc. SPIE 6142, 61421C (2006).
- [8] Cai, W., Ning, R. and Conover, D., "Scatter correction using beam stop array algorithm for cone-beam CT breast imaging," Proc. SPIE 6142, 61423E (2006).
- [9] Tischenko, O., Xu, Y. and Hoeschen, C., "A new scanning device in CT with dose reduction potential," Proc. SPIE 6142, 61422L (2006).
- [10] de las Heras, H., Tischenko, O., Renger, B., Xu, Y. and Hoeschen, C., "Experimental proof of an idea for a CT-scanner with dose reduction potential," these proceedings. SPIE (2008).
- [11] Xu, Y., Tischenko, O. and Hoeschen, C., "A new reconstruction algorithm for radon data," Proc. SPIE 6142, 61422A (2006).
- [12] Xu, Y., "A direct approach for reconstruction of images from Radon projections," Adv. in Appl. Math. 36, 2388–2420 (2006).
- [13] Kawrakow, I. and Rogers, D. W. O., [The EGSnrc code system: Monte Carlo simulation of electron and photon transport], PIRS Report 701, National Research Council of Canada, Ottawa, Canada (2003).
- [14] King, L. V., "Absorption problems in radioactivity," Phil. Mag. 23, 242–250 (1961).
- [15] International Electrotechnical Commission (IEC), [Medical electrical equipment Characteristics of digital X-ray imaging devices Part 1: Determination of the detective quantum efficiency], IEC 62220-1. Geneva, Switzerland (2003).
- [16] Sijbers, J. and Postnov, A., "Reduction of ring artifacts in high resolution micro-CT reconstructions," Phys. Med. Biol. 49, N247–N253 (2004).

Proc. of SPIE Vol. 6913 691352-10